

PAPER

[View Article Online](#)
[View Journal](#) | [View Issue](#)Cite this: *Mater. Adv.*, 2024,
5, 2377**CeO₂-promoted Cu₂O-based catalyst sprayed on the gas diffusion layer for the electroreduction of carbon dioxide to ethylene†**A. Alarcón, *^{ac} T. Andreu ^{ab} and C. Ponce de León ^c

The development of efficient and selective catalysts for the carbon dioxide reduction reaction (CO₂RR) is crucial for sustainable energy and chemical synthesis. In this work, CeO_{2-y} (y = C (cubic) and R (rod)) was incorporated into Cu₂O nanocube electrocatalyst as a promoter for ethylene (C₂H₄) production. The results demonstrate that the catalyst with a loading of 5 wt% crystalline CeO_{2-C} exhibits competitive activity and stability for ethylene production compared to pristine Cu₂O. Under optimized reaction conditions of −250 mA cm^{−2} current density and 1 M KOH electrolyte, the Cu₂O–5CeO_{2-C} catalyst achieved a faradaic efficiency (FE) of ~53% for C₂H₄ production, while maintaining stability over a period of 120 minutes. In contrast, non-promoted Cu₂O exhibited a lower FE for C₂H₄ (~38%) and experienced partial deactivation after 45 minutes. The characterization of the catalysts before and after the reaction revealed that the interaction between Cu₂O and CeO_{2-C} creates intrinsic sites (Cu^x–CeO_{2-x}; Cu^x = Cu²⁺, Cu⁺, and Cu⁰) for the binding of CO₂ and H₂O molecules. Moreover, the Cu₂O–5CeO_{2-C} catalyst outperforms other reported systems in terms of FE and partial current density for C₂H₄ production. It requires a lower potential (−0.98 V vs. RHE) to operate at the same electrolyte concentration. This finding highlights the promising nature of Cu₂O–5CeO_{2-C} as an efficient and cost-effective catalyst for C₂H₄ production.

Received 15th November 2023,
Accepted 19th January 2024

DOI: 10.1039/d3ma01009k

rsc.li/materials-advances

Introduction

The electrochemical carbon dioxide reduction reaction (CO₂RR) has attracted enormous interest due to its mild reaction conditions and potential to be used for renewable electricity storage via the production of synthetic fuels. Particularly, the CO₂RR to ethylene (C₂H₄) aiming at high current densities and faradaic efficiencies (FE) is intensively studied because of the extremely high industrial value and the need to transition away from fossil fuel C₂H₄ production.¹ Copper-based (Cu,^{2–4} CuO^{5–8} and Cu₂O^{9–14}) electrodes are proven to be the most used heterogeneous catalysts that tend to produce hydrocarbons and oxygenate compounds with competitive activity. However, as multi-step electron and proton transfer processes are involved in C₂H₄ formation, hydrogen (H₂) and other by-products such as

methane (CH₄) will inevitably be produced during electrolysis. Therefore, the design of efficient catalysis systems specific for the CO₂RR to ethylene with both high selectivity and high FE as well as low overpotential is highly desirable.

Various catalyst design strategies have been reported to effectively regulate the selectivity of the CO₂RR.^{15–17} Notably, by altering the electronic structure of Cu-based catalysts by the addition of a second metal^{18–20} or metal oxide promoter²¹ phase provides a significant improvement for C₂H₄ production. Ceria (CeO₂) is widely used as a catalyst, support and promoter for a variety of heterogeneous catalytic reactions involving the hydrogenation of CO₂²² due to its acid–base and unique redox properties of oxygen storage and release.²³ The size and shape modification, surface/face reconstruction, and faceting of ceria at the nanoscale level can offer an important tool to govern activity and stability in these reactions.²⁴ Furthermore, strong interaction between noble metals and ceria leads to their higher dispersion, electronic modifications and enhanced catalytic activity.²⁵

Recently, the implementation of CeO₂ as a support material for the CO₂RR has been investigated by some researchers. For instance, a high methane (CH₄) faradaic efficiency (up to ~54% at −1.2 V vs. RHE) over Cu/CeO_{2-x} nanocrystalline heterodimers was reported by S. Varandili *et al.*²⁶ In another

^a *Facultat de Química, Universitat de Barcelona, Martí i Franquès, 1, Barcelona 08028, Spain. E-mail: a.alarcon@ub.edu*^b *Sustainable Electrochemical Processes, Universitat de Barcelona, 08028, Barcelona, Spain*^c *Electrochemical Engineering Laboratory, Energy Technology Research Group, Faculty of Engineering and Physical Sciences, University of Southampton, Highfield Campus, University Road, Southampton, SO17 1BJ, UK*† Electronic supplementary information (ESI) available. See DOI: <https://doi.org/10.1039/d3ma01009k>

study, Cu/CeO₂ carbon nanofiber (Cu/CeO_x@CNF) catalysts synthesized by an electrospinning method were explored by X. Zong *et al.*²⁷ In this case, their optimized Cu/CeO_x@CNF_{S-2} catalyst exhibited a high CO faradaic efficiency (up to ~59% at -0.6 V vs. RHE) at a high current density of 100 mA cm⁻². Most recently, Zhao *et al.*²⁸ have that the Cu electrode coating with CeO₂ nanoparticles largely enhanced the C₂₊ product selectivity during CO₂ electroreduction. The FE and partial current density of C₂₊ products on the CeO₂-Cu electrode achieved in a gas-tight H-type electrolytic cell with 0.1 M KHCO₃ was 61% and 8.45 mA cm⁻² at -1.05 V vs. RHE, respectively. In that study, 1.5 mg cm⁻² was found to be the optimal CeO₂ coating. The improved CO₂RR selectivity and activity of CeO₂-Cu were attributed to the interface between Cu and CeO₂, which promotes C-C coupling towards C₂₊ production products. The CO₂RR to C₂₊ has also been evaluated over a CuO modified 20 wt% CeO₂ catalyst using a flow cell at 1 M KOH. Under those conditions, the reported faradaic efficiency of the C₂₊ products was ~75.2% at a current density of 1.21 A cm⁻². S. Yan *et al.*²⁹ revealed that CeO₂ and Cu and the subsurface Cu₂O coexisted in CeO₂/CuO during the CO₂RR and two competing pathways for C-C coupling were promoted separately, of which hydrogenation of *CO to *CHO is energetically favoured.

In terms of the CO₂RR to C₂H₄, the stabilization of Cu⁺ within a CuO-CeO₂ interface has been reported by S. Chu *et al.*³⁰ They suggested that tuning the CuO/CeO₂ interfacial interaction permits dramatic suppression of proton reduction and enhancement of CO₂ reduction. The C₂H₄ faradaic efficiency (up to ~50% at -1.1 V vs. RHE) was obtained over an optimised CuO/30 wt% CeO₂ using a liquid H-type cell with continuous CO₂ bubbling in 0.1 M KHCO₃ electrolyte. Lately, the effect of exposed facets of CeO₂ (cubes (100), rods (110), and octahedral (111)) has also been investigated under similar reaction conditions by S. Chu *et al.*³¹ In the CeO₂-supported Cu nanoparticles, they found that CeO₂ changed the oxidation state of Cu atoms towards Cu⁺ at the CuO-CeO₂ interface. This fact was mainly identified on the Cu/CeO₂(110), flowed by Cu/CeO₂(100) and Cu/CeO₂(111). The existence of Cu⁺ species was supposed to be likely the adsorption and active sites for CO₂ activation followed by further C-C coupling to yield C₂H₄. The FE towards C₂H₄ was ~39% on the Cu/CeO₂(110) at a mild overpotential of 1.13 V. In another study performed on a flow-cell at high current density and under 1 M KOH, Ce-doped Cu nanoparticles (Ce-Cu NPs) were reported to be highly selective to C₂H₄. A high faradaic efficiency (FE) of C₂H₄ close to 53% at a current density of 150 mA cm⁻² was achieved using a Ce/(Cu + Ce) precursor ratio = 10%. J. Shan *et al.*³² suggested that the high performance, which is 2.8 times higher than Cu nanoparticles under the same conditions, is due to the shrinking of the particle sizes due to Ce doping resulting in more catalytic active sites with oxygen defects. It seems that the proximity of the Ce atoms can boost the local electronic distribution on the Cu nanoparticles. Under similar reaction conditions, anchoring CeO₂ quantum dots on to the CuO surface has been evaluated by S. Wang *et al.*³³ Their optimal catalyst consisting of 100 wt% CeO₂ and 50 wt% CuO achieved a high faradaic efficiency of

~50% for ethylene with a partial current density of 197 mA cm⁻², attributed to the CuO/CeO₂ interfaces that simultaneously stabilize Cu⁺ and key intermediates.

Despite these advances in CuO supported CeO₂ electrocatalysts for CO₂RR to C₂H₄, the role of the CeO₂ as a promoter using Cu₂O instead of CuO has not been investigated yet. Recent studies have revealed that the Cu₂O phase provides a higher selectivity to ethylene compared to CuO.³⁴ Furthermore, the economic viability of most large-scale chemical processes relies on the use of simple and low-cost catalytic materials. Therefore, the implementation of CeO₂ as a promoter instead of bulk support is a practical way to design cost-effective electrocatalytic materials. In this line, the promoter content optimization into Cu₂O can provide a highly active-stable, and low-cost electrocatalytic formulation for C₂H₄ production.

Here, we developed a CeO₂-promoted Cu₂O-based catalyst sprayed on a carbon-based gas diffusion layer for the CO₂RR to C₂H₄. A series of Cu₂O-*x*CeO₂ were synthesized by the simple liquid phase reduction method. The influence of CeO₂ crystallinity and promoter loading (*x* = 5–20 wt%) was studied under relevant reaction conditions (current density (*j*) = -[50–300] mA cm⁻², 1 M KOH, and flow of CO₂ (*F*_{CO₂}) = 200 mL min⁻¹). Furthermore, the influence of the KOH concentration (0.1–3 M) and electrolyte type (KOH, KCl, and KHCO₃) over the optimized Cu₂O-5CeO₂ GDE was investigated to identify the best reaction components. Lastly, its stability was additionally tested under the selected reaction conditions (*j* = -250 mA cm⁻², electrolyte = 1 M KOH, and *F*_{CO₂} = 200 mL min⁻¹). The physico-chemical properties responsible for catalyst performance were studied using scanning electron microscopy-energy dispersive X-ray spectroscopy (SEM-EDX), transmission electron microscopy (TEM), X-ray diffraction (XRD), and Raman and photoelectron spectroscopy (XPS).

Experimental section

Chemicals and reagents

All chemical reagents used were of analytical grade without further treatment. Copper(II) sulfate [CuSO₄, 99%] and Nafion[®] perfluorinated resin solution (5 wt% in a mixture of lower aliphatic alcohols and water, 45% water) were purchased from Sigma Aldrich. Cerium(III) nitrate hexahydrate [Ce(NO₃)₃·6H₂O, 99.5%] was purchased from Thermo Scientific. L(+)-Ascorbic acid [C₆H₈O₆, 99%] was purchased from Acros Organics. Sodium hydroxide [NaOH, 97%], potassium hydroxide [KOH], and ethanol absolute [C₂H₆O, 99.8%] were purchased from Fisher Scientific. Ultrapure water was provided by Milli-Q Millipore source (18.2 MΩ cm, 20 °C).

Preparation of the catalysts

The promoter phase, CeO₂, was first synthesized using a hydrothermal method. In a typical synthesis, 3.25 g of Ce(NO₃)₃·6H₂O was dissolved in 15 mL of deionized water to obtain cerium nitrate aqueous solution. Then, a NaOH aqueous solution was prepared in a Teflon-lined steel reactor using 9 g



of NaOH and 50 mL of deionized water. The cerium nitrate aqueous solution was later added dropwise into the NaOH aqueous solution. After magnetic stirring for 30 min, the reactor was sealed and heated at two different temperatures of 80 °C and 240 °C for 24 h to obtain rod (R) and cubic (C) ceria particles, respectively. After cooling down to room temperature, the resulting precipitate was separated by centrifugation (4000 rpm for 5 min) and washed three times with excess ethanol, followed by drying in an oven overnight at 80 °C.

The series of CeO₂-promoted Cu₂O (Cu₂O-*x*CeO_{2-y}; *x* = 5, 10, 15 and 20 wt% and *y* = rod (R) and cubic (C) shape) samples were synthesized using a simple liquid phase reduction method. CuSO₄ (0.2689 g) and the respective amount of the promoter (CeO₂) were dissolved into 50 mL of distilled water under sonication for 30 min and later by magnetic stirring for 30 min. Sequentially, 0.8 g NaOH was dissolved in 50 mL of distilled water and added to the mixture dropwise. In the next step, 0.7045 g of C₆H₈O₆ as a reducing agent, was added to the mixture and kept constantly stirring for 30 min. Then, the CeO₂-promoted Cu₂O catalysts were centrifuged at 4000 rpm for 5 min and washed three times with excess ethanol. Finally, they were dried overnight in an oven at 80 °C. A non-promoted Cu₂O was also synthesized using the same procedure.

Preparation of gas diffusion electrode (GDE)

The GDE usually consists of a gas diffusion layer (GDL) on which a catalytic layer is deposited. The carbon-based GDL (Freudenberg H23C6) was used as the support. A catalytic ink was formulated by mixing 20 mg of the as-prepared catalyst, 0.5 mL of ethanol absolute and 140 µL of Nafion[®] perfluorate. The ink deposition on the GDL was performed using the spray coating technique. The catalyst loading mass was fixed to 1 ± 0.05 mg cm⁻² according to the previous control test, see Fig. SI1 (ESI[†]). After the catalyst deposition, GDEs were dried at room temperature. The GDEs were denoted as Cu₂O, Cu₂O-5CeO_{2-C}, Cu₂O-10CeO_{2-C}, Cu₂O-15CeO_{2-C}, Cu₂O-20CeO_{2-C}, CeO_{2-C}, Cu₂O-5CeO_{2-R}, and CeO_{2-R}. Fig. SI2 (ESI[†]) shows a systematic representation of the catalyst and GDE preparation.

CO₂ electroreduction set-up

The electrocatalytic tests were carried out using a compact H-type electrochemical cell.³⁵ The cell is shown in Fig. SI3 (ESI[†]), and included a current collector made of stainless steel with a built-in spiral flow field, which connected the cathode compartment and the GDE of the cell and guaranteed homogeneous distribution of the inlet reactants. In the first series of experiments, the influence of the promoter phase (CeO₂) was investigated using a CO₂ flow rate of 200 mL min⁻¹, which was adjusted by a manual flow meter (FR2000, Key Instruments). The working gas diffusion electrodes had a projected area of 1 cm² to the 1 M KOH aqueous electrolyte, while a platinum square mesh of 1 × 1 cm² was used as the counter electrode, located at the anode compartment and separated from the catholyte compartment by a proton exchange membrane (PEM, Nafion[®] 115) and immersed in 1 M KOH aqueous electrolyte. The total volume of the electrolyte was 150 mL. The reference

electrode was an Hg/HgO (1 M NaOH) electrode. The potential values were then translated into RHE (reversible hydrogen electrode) voltages by using eqn (1) and verified by a hydrogen reference electrode (Hydroflex[®] (M-v01-0071)).

$$E(\text{vs. RHE}) = E\left(\text{vs. } \frac{\text{Hg}}{\text{HgO}}\right) + 0.14 \text{ V} + 0.059 \text{ V} \times \text{pH} \quad (1)$$

For each electrode, the faradaic efficiency (FE) was evaluated by varying the current density from -50 to -300 mA cm⁻² ($\Delta j = -50 \text{ mA cm}^{-2}$) and using cronopotentiometry (PGSTAT204, Metrohm-Autolab). At each current density, the presence of gas products from the cathode outlet stream was examined for 5 minutes. During this time, the volume of the outlet products was measured and then analysed using an on-line gas chromatography (Shimadzu GC 2030) equipped with a Porapak Q 80/100 column. The gases (H₂, CO, CH₄ and C₂H₄) were detected using a thermal conductivity detector (TCD) and a flame ionization detector (FID).

After the identification of the most promising Ce-promoted copper-based GDE, the influence of the KOH concentration (0.1 M–3 M) and electrolyte type (KCl, KOH, KHCO₃) over the optimized Cu₂O-5CeO_{2-C} GDE was additionally investigated to find the most effective electrolyte conditions. Finally, a stability test was performed at the selected reaction conditions ($j = -250 \text{ mA cm}^{-2}$, electrolyte = 1 M KOH, $F_{\text{CO}_2} = 200 \text{ mL min}^{-1}$).

The FE_X of the X obtained products, such as C₂H₄, CH₄, CO and H₂, were estimated by using the following equation (eqn 2):

$$\text{FE}_X = \frac{Q_X}{Q_{\text{Total}}} = \frac{n_X N_X F}{Q_{\text{Total}}} \quad (2)$$

where Q_X and Q_{Total} are the charge passed to produce product X and the total passed charge (C) during CO₂RR, n_X represents the electron transfer number of product X, N_X is the product amount (mol) of X measured by the GC, and F is the Faraday constant (96 485 C mol⁻¹).

Catalyst characterization

The series of catalysts sprayed on the carbon-based gas diffusion layer were characterized by different physico-chemical techniques like scanning electron microscopy-energy dispersive X-ray spectroscopy (SEM-EDX), transmission electron microscopy (TEM), X-ray diffraction (XRD), and Raman and photoelectron spectroscopy (XPS).

The surface morphology and elemental composition were investigated using a JEOL JSM-7200F high-resolution SEM equipped with an EDX detector (Oxford instruments) and AZtecEnergy software. Prior to EDX analysis, catalysts were fixed over an aluminium holder. Elemental analysis was carried out at 20 kV and restricted to Cu, Ce, and O to avoid inconsistent results. TEM images were recorded on a FEI Tecnai T12 electron microscope operating at 120 kV. The powder samples were dispersed by ultrasound in ethanol. Suspension drops were deposited on a holey carbon-coated copper grid of 300 mesh and then dried in air.

The crystal structure of the catalysts was examined using a Bruker type XRD D2 Phaser diffractometer. X-ray powder



diffraction patterns were acquired by applying a Cu K α radiation ($\lambda = 1.5406 \text{ \AA}$), a voltage of 40 kV, and a current of 40 mA. Continuous scans were collected over the 2θ range of 10° to 80° . The crystalline phases present in the samples were identified by comparison with reference patterns available in the JCPDS database. The crystallite sizes of the main Cu x species (Cu $_2$ O, CuO and Cu 0) and cerium oxide (CeO $_2$) were estimated using the Scherrer's equation at $2\theta = 36.46^\circ$ for Cu $_2$ O (111), 38.76° for CuO (111), 43.32° for Cu (111), and 28.53° for CeO $_2$ (111); $D = (K\lambda/\beta \cos \theta)$, where λ is the X-ray wavelength, β is the full width of the diffraction line at half maximum (FWHM), and θ is the Bragg angle.

Raman measurements were recorded on a Raman spectrometer (Horiba LabRAM HR800) equipped with a CCD detector, using a laser with a wavelength of 532 nm as the excitation source. The Raman spectra were obtained using a x50LWD objective with an incident power of 0.1 mW (5 acquisitions, 60 s of exposure time).

X-ray photoelectron spectroscopy (XPS) experiments were performed in a PHI 5500 Multitechnique System (from Physical Electronics) with a monochromatic X-ray source (Al K α 1486.6 eV).

Results and discussion

Characterization

SEM images displayed in Fig. SI4 (ESI †) evidenced that the formation of particles with cubic-like morphology was achieved for both the active phase (Cu $_2$ O) and promoter phase (CeO $_2$ -C) prepared at 240°C . In the case of CeO $_2$ -R prepared at 80°C , its morphology was not possible to identify by SEM because the particle sizes were below the detection limits. When the electrocatalysts were synthesised in the presence of CeO $_2$ -C, a catalytic system composed of particles with a cubic shape was also achieved for the series of CeO $_2$ -C-promoted Cu $_2$ O-based catalyst. Furthermore, EDX analysis performed over all catalysts proved the presence of their main components (Cu, Ce, and O). As a representative example, the EDX elemental mapping image exhibited in Fig. 1 demonstrated the experimental composition (82 wt% Cu, 5 wt% Ce, and 13 wt% O) and interaction between the cubic particles of the Cu $_2$ O-5CeO $_2$ -C catalyst.

A summary of the elemental composition of all the as-prepared catalysts is shown in Table 1. The experimental composition of the CeO $_2$ promoter phase falls within the range of $6\text{--}21 \text{ wt}\% \pm 1$, which closely matches the theoretical values. On the other hand, a slight difference in the elemental composition was mainly identified between the two synthesized promoters (CeO $_2$ -R (81 wt% Ce and 19 wt% O) and CeO $_2$ -C (83 wt% Ce and 17 wt% O)), suggesting the possible presence of different oxidation state of cerium (Ce $^{3+}$ and Ce $^{4+}$) over these samples. Therefore, the used temperature for the synthesis of CeO $_2$ nanoparticles can be a key parameter for the generation of Ce $^{3+}$ and Ce $^{4+}$.

The cubic-like morphology of the CeO $_2$ -C promoter (Fig. 2(a)) and pristine Cu $_2$ O (Fig. 2(b)) was additionally confirmed by

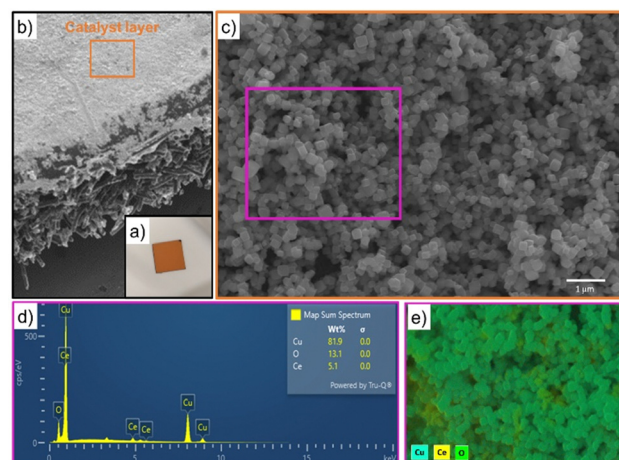


Fig. 1 Surface morphology and elemental composition analysis for the Cu $_2$ O-5CeO $_2$ -C GDE. (a) Image of the as-prepared GDE. (b) SEM image showing the catalyst layer and the carbon-based GDL. (c) SEM image of the electron micrograph region, (d) EDX spectrum, (e) and distribution of Cu, Ce and O in elemental mapping.

Table 1 Elemental composition of the catalysts

Sample	Elemental composition		
	Cu	Ce	O
	[wt% ± 2]		
Cu $_2$ O	89	—	11
Cu $_2$ O-5CeO $_2$ -C	82	5	13
Cu $_2$ O-10CeO $_2$ -C	75	9	16
Cu $_2$ O-15CeO $_2$ -C	70	12	18
Cu $_2$ O-20CeO $_2$ -C	62	17	21
CeO $_2$ -C	—	83	17
CeO $_2$ -R	—	81	19
Cu $_2$ O-5CeO $_2$ -R	81	4	15

TEM. Regarding the CeO $_2$ -R, rod-like morphologies with particle sizes of $\sim 8 \text{ nm}$ and irregular length can be identified, see Fig. SI5 (ESI †). Between cubic particles, the main difference observed was the size. The cubic CeO $_2$ -C particles ($\sim 29 \text{ nm}$)

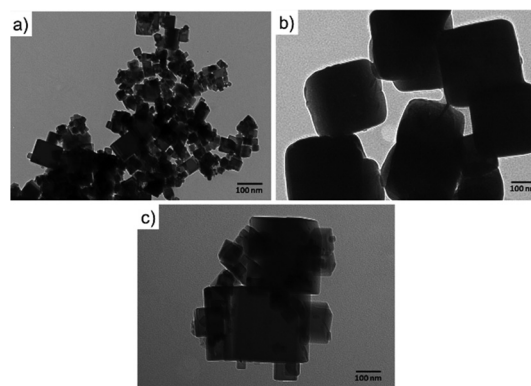


Fig. 2 TEM images of the (a) CeO $_2$ -C, (b) Cu $_2$ O, and (c) Cu $_2$ O-5CeO $_2$ -C catalysts.



were smaller than cubic Cu_2O particles (~ 165 nm). The interaction between the $\text{CeO}_{2-\text{C}}$ and Cu_2O particles was clearly detected over a series of Cu_2O - $\text{CeO}_{2-\text{C}}$ catalysts. Fig. 2(c) is an example of the strong Cu_2O - CeO_2 interaction achieved over the Cu_2O catalyst promoted by 5 wt% $\text{CeO}_{2-\text{C}}$. For this $\text{CeO}_{2-\text{C}}$ -promoted Cu_2O catalyst, a decrease in the Cu_2O particle sizes was found, suggesting that the addition of CeO_2 during the synthesis inhibits the growth of Cu_2O particles. The average particle sizes estimated for $\text{CeO}_{2-\text{C}}$ and Cu_2O were 43 nm and 160 nm, respectively.

The XRD patterns of the $\text{CeO}_{2-\text{C}}$ promoter, pristine Cu_2O and the series of $\text{CeO}_{2-\text{C}}$ -promoted Cu_2O are shown in Fig. 3. The XRD profiles confirmed the phase purity of the polycrystalline CeO_2 (JCPDS: 00-034-0394) and Cu_2O (JCPDS: 00-005-0667). For the $\text{CeO}_{2-\text{C}}$ sample, the high-intensity reflections are observed at $2\theta = 28.53, 33.09, 47.48, 56.33, 59.08, 69.41, 76.69$, and 79.04° corresponding to the CeO_2 (111), (200), (220), (311), (222), (400), (331), (420) lattice planes. On the other hand, the diffraction peak at around $2\theta = 29.61, 36.46, 42.34, 61.42$, and 73.56° represent the Cu_2O (110), (111), (200), (220), and (311) lattice planes. Over the series of Cu_2O - $\text{CeO}_{2-\text{C}}$ catalysts, CeO_2 and Cu_2O reflections were identified at a similar 2θ position, but with differences in their relative intensity, in agreement with the composition. With higher CeO_2 content, the intensity of the reflections of CeO_2 increased, while the reflections of Cu_2O were decreased. Compared to $\text{CeO}_{2-\text{C}}$ promoter, the XRD profiles of $\text{CeO}_{2-\text{R}}$ suggested that the sample appeared to be composed of small particles. Only four reflections were identified for the $\text{CeO}_{2-\text{R}}$. As can be seen in Fig. S16 (ESI[†]), the reflections related to CeO_2 phase in the Cu_2O - $\text{CeO}_{2-\text{R}}$ were under the detection limit. These reflections were identified at $2\theta = 28.53, 33.09, 47.48, 56.33^\circ$ and associated to the CeO_2 (111), (200), (220), (311) lattice planes.

On the other hand, Raman spectroscopy analysis was additionally performed over the most promising fresh samples ($\text{CeO}_{2-\text{C}}$, Cu_2O , and Cu_2O -5 $\text{CeO}_{2-\text{C}}$) taking into consideration that the formation of defective sites can be interpreted by the alteration in M-O vibration frequency after CeO_2 introduction to the Cu_2O structure. Fig. 4 proved that the fluorite-type cubic

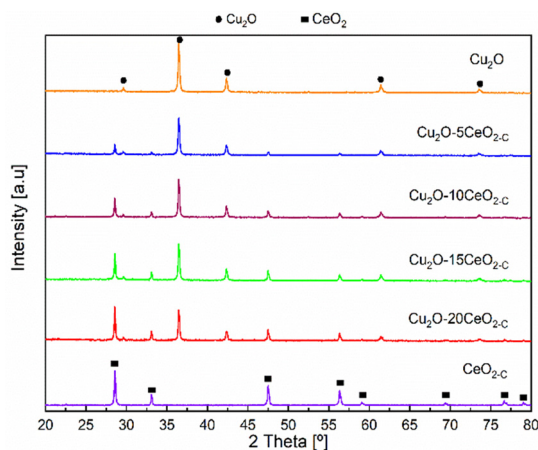


Fig. 3 XRD Patterns of the catalysts.

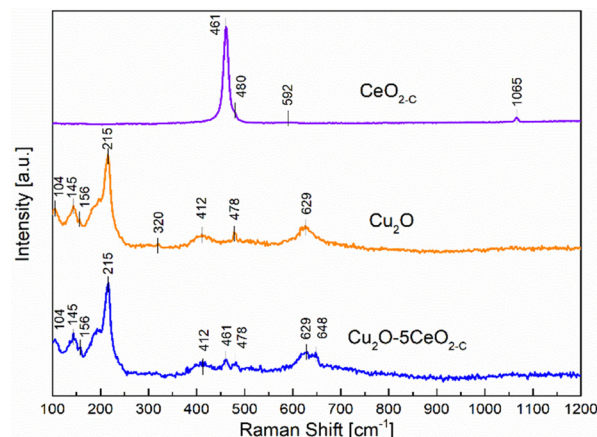


Fig. 4 Raman spectrum of $\text{CeO}_{2-\text{C}}$, Cu_2O and Cu_2O -5 $\text{CeO}_{2-\text{C}}$ catalysts.

crystal structure of ceria in the $\text{CeO}_{2-\text{C}}$ sample exhibits one first-order Raman active fundamental mode located at 461 cm^{-1} .³⁶ This F_{2g} mode was associated with the symmetric vibrations of oxygen ions around Ce^{4+} ions in octahedral $\text{Ce}-\text{O}_6$.³⁷ The bands at 480 and 592 cm^{-1} were attributed to the oxygen vacancies due to the presence of reduced Ce^{3+} cations (Ce^{3+}O_6)³⁸ and the vacancy-interstitial Frenkel-type oxygen intrinsic defects in pure ceria,³⁹ respectively. Additionally, solid-state phonons assigned to second-order features $2\omega\text{R}(\text{X})$ were observed at 1065 cm^{-1} .⁴⁰

In the non-promoted Cu_2O sample, the most intense Raman peak identified at 215 cm^{-1} was related to the second-order overtone $2\Gamma_{12}^-$.⁴¹ The remaining Raman bands were assigned as follows: an inactive mode Γ_{12}^- at 104 cm^{-1} , an IR active mode $\Gamma_{15}^{(1)}$ (LO) at 145 cm^{-1} , a fourth order overtone $4\Gamma_{12}^-$ at 412 cm^{-1} , and an IR active mode $\Gamma_{15}^{(1)}$ (TO) at 629 cm^{-1} .⁴²⁻⁴⁴ In addition to the prominent peaks observed for Cu_2O , a weak band was also observed at 320 cm^{-1} , which corresponds to the A_g mode of CuO .⁴⁵ On the other hand, the introduction of CeO_2 into the Cu_2O structure induced the formation of a new extrinsic MO_8 site capable of delivering oxygen under reducing conditions, *i.e.* part of a Frenkel defect.⁴⁶ This new Raman peak identified over the Cu_2O -5 $\text{CeO}_{2-\text{C}}$ catalyst located at 648 cm^{-1} can be probably an effect of the strong interaction between Cu^+ and Ce^{3+} cations.⁴⁷ Furthermore, the presence of the CuO phase was not identified in comparison with the Cu_2O sample, implying that CeO_2 avoids overoxidation of Cu_2O and preserves the $\text{Cu}(\text{i})$ oxidation state.

The surface elemental composition and chemical state of the fresh $\text{CeO}_{2-\text{C}}$, Cu_2O and Cu_2O -5 $\text{CeO}_{2-\text{C}}$ samples were examined by X-ray photoelectron spectroscopy. The survey scan in Fig. S17 (ESI[†]) shows the presence of C, Cu, Ce and O. The C 1s peak at 284.4 eV was used as a reference peak for calibration of all the spectra. The high-resolution XPS spectra of Cu 2p are presented in Fig. 5. The peaks at 932.1 eV and 951.9 eV were linked to $\text{Cu}^+ 2p_{3/2}$ and $\text{Cu}^+ 2p_{1/2}$, respectively. Furthermore, characteristic shoulder peaks can also be resolved at 934.8 and 954.8 eV , which were associated with $\text{Cu}^{2+} 2p_{1/2}$ and $\text{Cu}^{2+} 2p_{3/2}$, respectively. The presence of satellite peaks at the binding

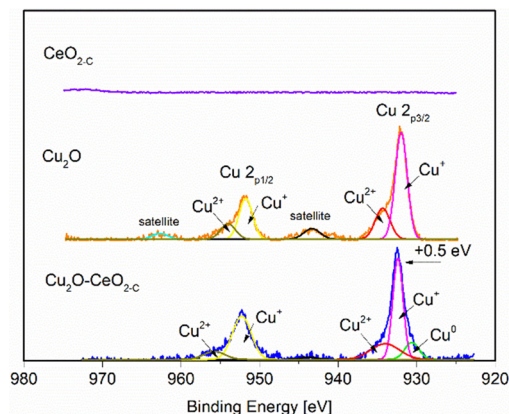


Fig. 5 Cu 2p XPS spectra of $\text{CeO}_{2-\text{C}}$, Cu_2O and $\text{Cu}_2\text{O}-5\text{CeO}_{2-\text{C}}$ catalysts.

energies of 943.4 indicated that Cu(I) was the major valence state for Cu species.⁴⁸

The peaks of the $\text{Cu}_2\text{O}-5\text{CeO}_{2-\text{C}}$ nanocomposites shift in the direction of high binding energy compared with that of the Cu_2O nanocrystals. The difference between the two peaks is 0.5 eV from the binding energy, which indicates that there is an electronic exchange between Cu_2O and CeO_2 . In particular, the Cu^0 phase was identified in the $\text{Cu}_2\text{O}-5\text{CeO}_{2-\text{C}}$ sample, suggesting that CeO_2 promotes the reduction of CuO . Regarding the CeO_2 phase (see Fig. S18, ESI[†]), peaks at 881.9, 888.1, 897.9,

899.8, 901.8, and 916.1 eV were only detected in the Ce 3d spectrum of the CeO_2 sample, corresponding to the binding energies of $\text{Ce}^{4+} 3d_{5/2}$, $\text{Ce}^{3+} 3d_{5/2}$, SU_1 , $\text{Ce}^{4+} 3d_{3/2}$, SU_2 , and $\text{Ce}^{3+} 3d_{3/2}$, respectively.⁴⁹ Fig. S19 (ESI[†]) depicts the high-resolution O 1s spectra of the different catalysts. The characteristic peaks resolved in the binding energy range of 534.6 to 526.3 eV were assigned to lattice oxygen (O_{lat}) and oxygen vacancies (O_{Vs}).^{50,51} Compared to Cu_2O , the relative proportion of oxygen vacancies was higher for the $\text{Cu}_2\text{O}-5\text{CeO}_2$. The O_{Vs} are renowned for their possession of weakly bound electrons, serving as exceptional Lewis base sites for CO_2 adsorption. These electrons contribute to the formation of the $\text{CO}_2^{\bullet-}$ intermediate by providing electron donation.^{52,53} Therefore, this indicates that the $\text{Cu}_2\text{O}-5\text{CeO}_2$ exhibits the strongest ability for CO_2 adsorption and subsequent electrochemical reduction.

CO_2RR

CeO_2 loading. Fig. 6 illustrates the influence of $\text{CeO}_{2-\text{C}}$ loading on a series of Cu_2O -based gas diffusion electrodes (GDEs). During the CO_2 electroreduction reaction in 1 M KOH, the main products detected across all GDEs were C_2H_4 , CH_4 , CO , and H_2 . Within the evaluated range of current densities (-50 to -300 mA cm^{-2}), the faradaic efficiencies for C_2H_4 production were consistently higher in the $\text{CeO}_{2-\text{C}}$ -promoted Cu_2O -based GDEs compared to the non-promoted

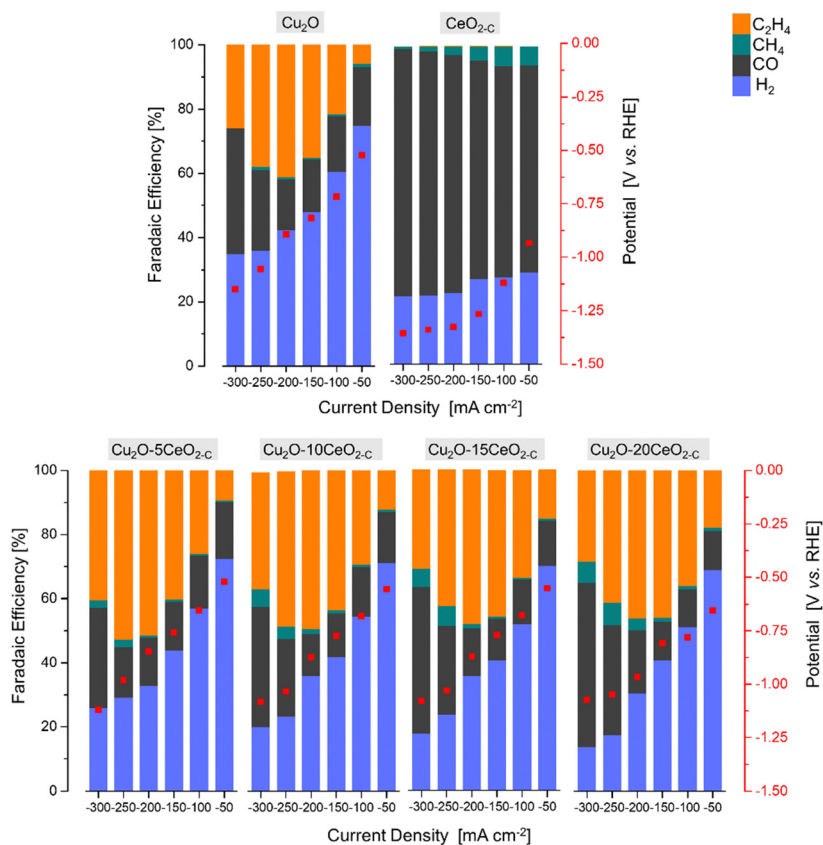


Fig. 6 The faradaic efficiency [%] and potential [V vs. RHE] as a function of the current density [mA cm^{-2}] over the series of Cu_2O -based GDEs.



Cu₂O GDE. This indicates that the incorporation of the CeO_{2-C} promoter phase is beneficial for enhancing C₂H₄ formation during the CO₂RR.

The product formation on the CeO_{2-C} electrode starts at approximately -0.93 V vs. RHE, see Fig. 6. The achieved faradaic efficiencies (FEs) for C₂H₄ were lower compared to the FEs for other sub-products such as H₂, CO, and CH₄. The maximum FE_{C₂H₄} observed for this electrode was 0.6% at -1.34 V vs. RHE, and this was achieved at a high current density ($j = -250$ mA cm⁻²). In contrast, when the current densities exceeded -150 mA cm⁻², a noticeable increase in FE_{CO} ($>75\%$ at -1.33 V vs. RHE) and a decrease in FE_{CH₄} ($<3\%$ at -1.33 V vs. RHE) were observed. Comparing with the CeO_{2-C} electrode, the Cu₂O electrode exhibited a maximum FE_{C₂H₄} of approximately 41% at -0.87 V vs. RHE, which was achieved at a current density of -200 mA cm⁻². The onset potential for C₂H₄ formation (approximately -0.52 V vs. RHE) was lower compared to the CeO_{2-C} electrode.

The observed behaviour of faradaic efficiencies (FEs) for the Cu₂O–CeO_{2-C} series indicates that a lower amount of the CeO₂ promoter is favoured to enhance C₂H₄ production. In this case, the potential at which C₂H₄ formation starts ranged between -0.52 and -0.67 V vs. RHE. It is noteworthy that the maximum FEs for C₂H₄ were shifted towards lower current densities due to the increased CeO₂ loading. Furthermore, the FE_{CO} and FE_{CH₄} increased, while FE_{H₂} decreased with both increasing CeO₂ loading and current density. Among the Cu₂O–CeO_{2-C} electrodes, Cu₂O with 5 wt% of CeO_{2-C} was determined to be the optimum electrode for C₂H₄ production. It achieved a maximum FE_{C₂H₄} of approximately 53% at -0.98 V vs. RHE, at a current density of -250 mA cm⁻².

To investigate the influence of the CeO₂ particle morphology, a CO₂RR test was conducted using rod-like ceria particles (CeO_{2-R}) with the optimized promoter content of 5 wt% (previously found for cubic-like ceria particles, CeO_{2-C}), under the same reaction conditions (1 M KOH, $j = -50$ to -300 mA cm⁻²). Fig. SI10 and SI11 (ESI†) revealed that the FEs for C₂H₄

formation are dependent on the shape of the promoter particles.

In the CeO_{2-R} promoter electrode, the main products observed were CO, H₂, CH₄, and C₂H₄, similar to the CeO_{2-C} promoter. However, compared to CeO_{2-C}, the CeO_{2-R} electrode required a more negative potential (-0.94 V vs. RHE) to initiate C₂H₄ formation. Furthermore, the maximum FE for C₂H₄ ($\sim 0.15\%$ at -1.26 V vs. RHE) over CeO_{2-R} was detected at a current density of -150 mA cm⁻². This suggests that the rod-like ceria morphology is less favourable for C₂H₄ production, as a higher potential was achieved at relatively low current densities. Regarding the FEs for other subproducts, CeO_{2-R} exhibited a lower FE for CO and higher FE for H₂ and CH₄ compared to CeO_{2-C}, as shown in Fig. SI10 (ESI†).

On the other hand, the combination of Cu₂O with CeO_{2-R} did not have a positive effect on enhancing the faradaic efficiency for C₂H₄, see Fig. SI11 (ESI†). The maximum FE_{C₂H₄} achieved over the Cu₂O–CeO_{2-R} electrode was only $\sim 50\%$ at -0.90 V vs. RHE. This low faradaic efficiency can be attributed to the insignificant promotion of CO₂ and H₂O activation by the presence of CeO_{2-R}, as shown in Fig. SI9 (ESI†). Therefore, the results suggest that CeO_{2-C} promotes more suitable activation of both CO₂ and H₂O molecules, which is crucial for ensuring the selective formation of C₂H₄. It should be noted that the optimum catalyst exhibits a low cathodic polarization compared to pristine Cu₂O (Fig. SI12, ESI†) attributed to the local CO formation at the CeO_{2-C} promoter and simultaneous CO₂ and CO electroreduction. Thus, the combination of Cu₂O with CeO_{2-C} demonstrates improved performance in terms of FE_{C₂H₄} compared to Cu₂O–CeO_{2-R}.

Electrolyte. The influence of three different electrolytes, namely KOH, KCl, and KHCO₃, was investigated on the optimized Cu₂O–5CeO_{2-C} catalyst while maintaining a constant electrolyte concentration of 1 M and varying the current density ($j = -[50-300]$ mA cm⁻²). In terms of C₂H₄ production, the KOH electrolyte exhibited higher C₂H₄ faradaic efficiencies ($\geq 9\%$ at -0.52 V vs. RHE) at all tested current densities, except for 50 mA cm⁻². The selectivity trend for C₂H₄ among the

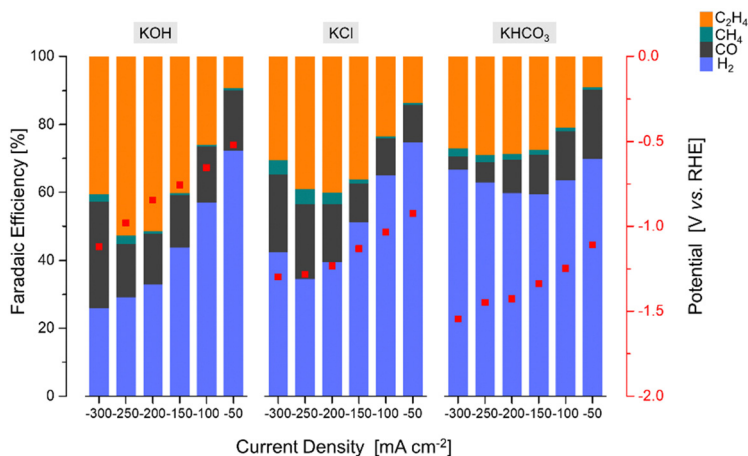


Fig. 7 The faradaic efficiency [%] and potential [V vs. RHE] as a function of current density [mA cm⁻²] over the Cu₂O–5CeO_{2-C} GDE using different electrolytes.



different electrolytes was observed as follows: $\text{KOH} > \text{KCl} > \text{KHCO}_3$, as shown in Fig. 7. As the current density increased, the preferential occurrence of the hydrogen evolution reaction was observed in the electrolytes based on KCl and KHCO_3 . Overall, KHCO_3 exhibited the most negative potentials (> -1.10 V vs. RHE) compared to the other evaluated electrolytes. Therefore, the selection of the electrolyte is crucial for the CO_2 reduction reaction on $\text{Cu}_2\text{O}-5\text{CeO}_{2-\text{C}}$ gas diffusion electrodes, with alkaline KOH conditions enabling preferential C_2H_4 production.

KOH concentration. As the electrolyte pH also plays an important role in the CO_2RR to C_2H_4 , the influence of the KOH concentration was evaluated by varying the current density ($j = -[50-300]$ mA cm^{-2}). Fig. 8 demonstrates that the electrochemical activity is highly dependent on the concentration of KOH. Notably, the lowest faradaic efficiencies for C_2H_4 production ($\geq 18\%$ at -0.60 V vs. RHE) were observed at the selected KOH concentration of 0.1 M. In contrast, there was an expected decline in the preference for the hydrogen evolution reaction with increasing concentration (> 1 M). Similarly, at higher current densities (> 250 mA cm^{-2}), the hydrogen evolution reaction became even less preferred. Concerning the potentials, more negative values (-1.05 V vs. RHE) were achieved with the increase of the KOH concentration. Particularly, CO and CH_4 were the main products promoted at those high negative potential values.

Stability test. The stability of $\text{Cu}_2\text{O}-5\text{CeO}_{2-\text{C}}$ and Cu_2O catalysts shown in Fig. 9 was used to evaluate the effect of the promoter phase. The tests were conducted under the optimized reaction conditions of $j = -250$ mA cm^{-2} and 1 M KOH electrolyte, which were found to yield the most promising results for the $\text{CeO}_{2-\text{C}}$ -promoted Cu_2O gas diffusion electrode (GDE). Under these selected conditions, the $\text{Cu}_2\text{O}-5\text{CeO}_{2-\text{C}}$ electrode exhibited a higher $\text{FE}_{\text{C}_2\text{H}_4}$ ($\sim 53\%$ at -0.98 V vs. RHE) and maintained its stability over a period of 120 minutes. The faradaic efficiencies for other byproducts (H_2 , CO, and CH_4) remained constant throughout the reaction (see Fig. SI13, ESI†).

In contrast, when using non-promoted Cu_2O , the initial $\text{FE}_{\text{C}_2\text{H}_4}$ reached a maximum value of approximately 38% at

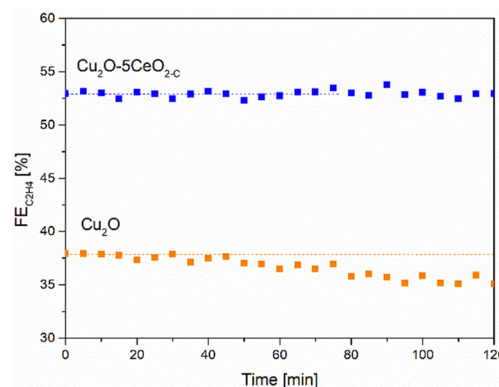


Fig. 9 C_2H_4 FE [%] as a function of the time [min] over the $\text{Cu}_2\text{O}-5\text{CeO}_{2-\text{C}}$ GDE. Reaction conditions: electrolyte = 1 M KOH and $j = -250$ mA cm^{-2} .

-1.05 V vs. RHE but experienced partial deactivation after 45 minutes. The FE for C_2H_4 on the Cu_2O electrode decreased by approximately 5% . Notably, the FEs for CO and H_2 increased as the FE for C_2H_4 and CH_4 decreased on Cu_2O (see Fig. SI14, ESI†).

Consistently with these experimental findings, the 5 wt% $\text{CeO}_{2-\text{C}}$ -promoted Cu_2O demonstrated enhanced performance compared to the non-promoted Cu_2O electrode in terms of ethylene production, aligning with the results obtained from linear sweep voltammetry (see Fig. SI15, ESI†). The $\text{Cu}_2\text{O}-5\text{CeO}_{2-\text{C}}$ electrode exhibited a more positive onset potential than Cu_2O , indicating that it was the most active catalyst for the CO_2RR .

XRD measurements were also conducted on the Cu_2O and $\text{Cu}_2\text{O}-5\text{CeO}_{2-\text{C}}$ gas diffusion electrodes at different reaction times ($t = 0$ (before reaction: fresh), 5 and 120 min (after reaction: used)) to investigate the surface copper species during the stability test. In both the fresh and used electrodes, reflections at 18.15 , 25.67 , and 52.74° were attributed to the carbon phase (JCPDS: $00-047-0787$ and $00-026-1076$) of the carbon-paper support (see Fig. SI16, ESI†). Prior to sample activation ($t = 0$ min), characteristic reflections associated with the Cu_2O

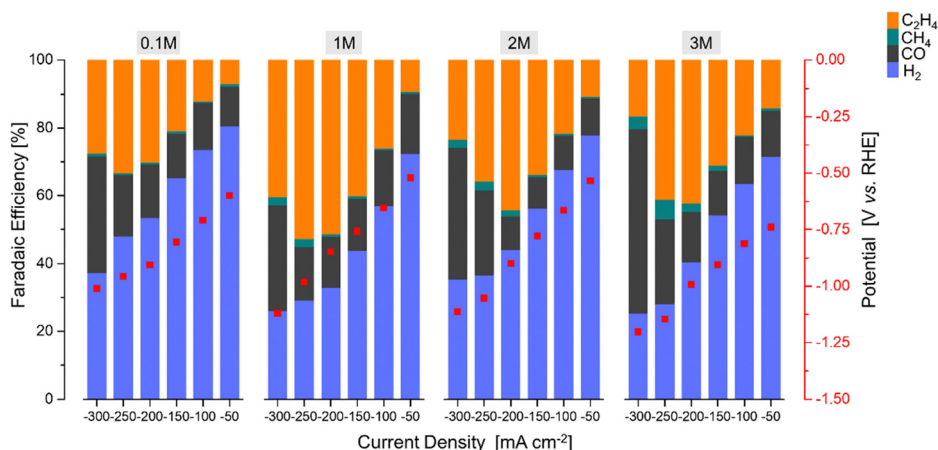


Fig. 8 The faradaic efficiency [%] and potential [V vs. RHE] as a function of the current density [mA cm^{-2}] over the $\text{Cu}_2\text{O}-5\text{CeO}_{2-\text{C}}$ GDE using different KOH concentrations.



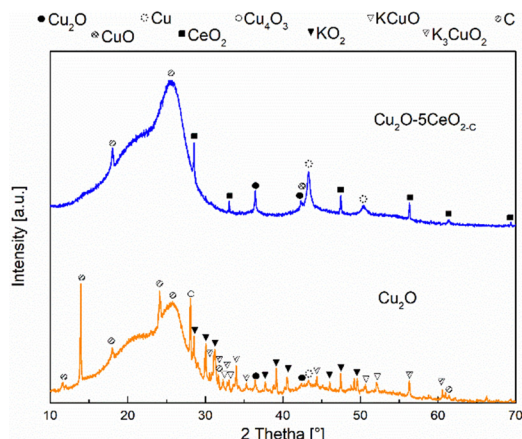


Fig. 10 XRD patterns of the Cu_2O and $\text{Cu}_2\text{O}-5\text{CeO}_2$ GDEs at the reaction time of 120 minutes.

phase were observed in both Cu_2O (see Fig. SI17, ESI†) and $\text{Cu}_2\text{O}-5\text{CeO}_2$ (Fig. SI18, ESI†) electrodes. Additionally, CeO_2 was detected on the $\text{Cu}_2\text{O}-5\text{CeO}_2$ electrode.

After a reaction time of 5 min, the intensity of reflections corresponding to Cu_2O decreased in both gas diffusion electrodes, and two new phases, CuO (JCPDS: 01-078-0428) and metallic Cu^0 (JCPDS: 00-004-0836), were identified. A similar behaviour was observed for the intensity of the reflections related to the CeO_2 phase in the $\text{Cu}_2\text{O}-5\text{CeO}_2$ electrode. However, two new phases, Cu_4O_3 (JCPDS: 00-033-0480) and K_3CuO_2 (JCPDS: 00-038-0971), were specifically identified in the Cu_2O electrode.

At a total reaction time of 120 min (see Fig. 10), the reflections corresponding to CuO phases disappeared, and the intensity of reflections related to Cu_2O and Cu^0 decreased. Additionally, new reflections were observed in the Cu_2O electrode, which were associated with the KCuO (JCPDS: 01-076-2437) and KO_2 (JCPDS: 01-084-1972) phases. In contrast, the reflections of $\text{Cu}_2\text{O}-5\text{CeO}_2$ remained like those identified at 5 min, indicating that CeO_2 promoted the stability of the main copper species (Cu_2O , CuO , and Cu^0) involved in the CO_2RR . These identified copper species were consistent with those detected through cyclic voltammetry measurements (see Fig. SI19, ESI†).

According to XRD analysis, the crystallite size of the main $\text{Cu}^x = \text{Cu}^{2+}$, Cu^+ , and Cu^0 species were modified after the reaction, see Table SI1 (ESI†). The increase of the Cu_2O crystallite size for the non-promoted Cu_2O catalyst was 15%, while for the $\text{Cu}_2\text{O}-5\text{CeO}_2$ it was 1%. For $\text{Cu}_2\text{O}-5\text{CeO}_2$, the CeO_2 crystallite sizes were also slightly increased by 8%. Furthermore, the crystallite size corresponding to the Cu phase (20 nm) was higher for the Cu_2O sample. Therefore, the poor stability of the Cu_2O catalyst can result in the increase of the crystallite sizes of the main copper species.

Additionally, SEM-EDS analysis was performed after the reaction to verify the catalyst composition, see Table SI2 (ESI†). Besides the main elements (Cu , Ce , and O), the potassium (K) phase was also detected on the surface of both used catalysts. However, a clear modification of the catalyst composition was identified for used Cu_2O . In this catalyst, the Cu phase decreased by 55% compared to its fresh estate. This behaviour

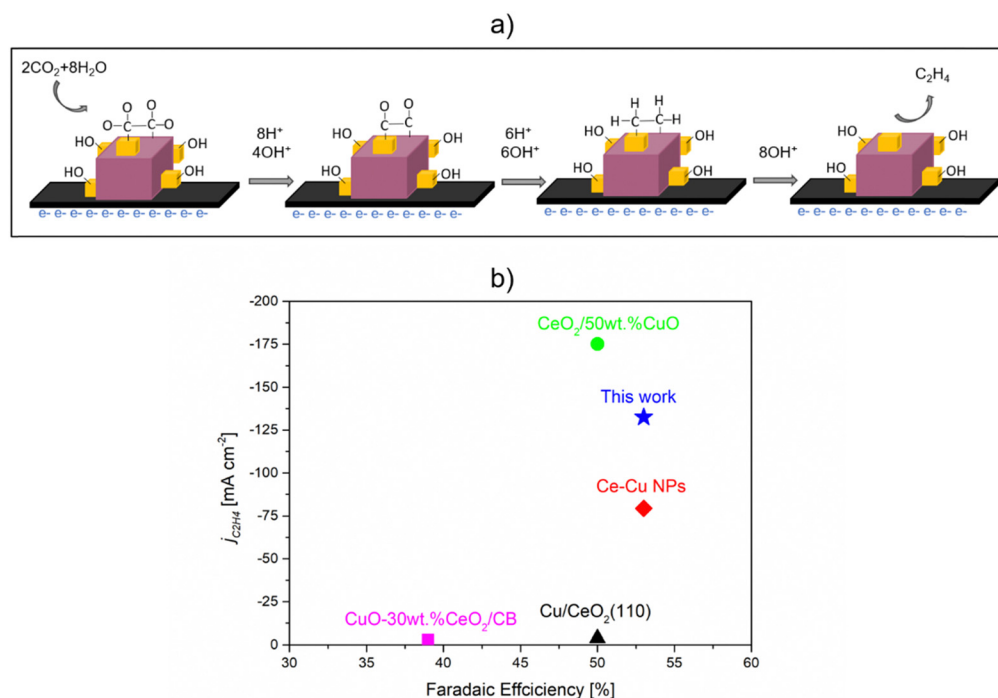


Fig. 11 CO_2RR to ethylene over $\text{Cu}_2\text{O}-5\text{CeO}_2$ GDE. (a) Plausible mechanism of CO_2RR to C_2H_4 . (b) Performance comparison with similar catalytic system reported in the literature. 0.1 M KHCO_3 was used for $\text{CuO-30 wt}\% \text{CeO}_2/\text{CB}$ ³¹ and $\text{Cu/CeO}_2(100)$,³¹ while 1 M KOH was used for $\text{CeO}_2/50 \text{ wt}\% \text{CuO}$,³³ Ce-Cu NPs ,³² and $\text{Cu}_2\text{O-5 wt}\% \text{CeO}_2$ (this work).

can be related to the presence of the new KOx and KCuOx phases (see Fig. SI20, ESI†), in agreement with post-catalysis XRD results. Regarding the used Cu₂O–5CeO₂, its composition was slightly modified, suggesting that CeO_{2-C} (see Fig. SI21, ESI†) inhibits the formation of potassium species, which are negative for ethylene production.

Based on the electrochemical and catalyst characterization conducted before and after the reaction, it can be concluded that the interaction between Cu₂O and CeO₂ creates intrinsic sites (Cu^x–CeO_{2-x}; Cu^x = Cu²⁺, Cu⁺, Cu⁰) for the binding of CO₂ and H₂O. The proposed mechanism, illustrated in Fig. 11(a), suggests that CO₂ can be adsorbed around the Cu^x–CeO_{2-x} interface and reduced to *CO on the CeO_{2-x} site. This step is crucial as CO serves as the key intermediate for the production of C₂₊ products.^{30,33} Subsequently, *CO can undergo further reduction to C₂H₄ through enhanced *CO–*CO coupling, which occurs on Cu^x = Cu²⁺, Cu⁺, and Cu⁰ sites, with the assistance of H⁺ species derived from adsorbed H₂O on Cu⁺–CeO_{2-x} sites.^{30,54} Therefore, the improved and stable FE_{C₂H₄} achieved with the Cu₂O–5CeO_{2-C} catalyst supports the assertion that CeO_{2-C} plays a significant role in the CO₂RR. It promotes the formation of Cu^x–CeO_{2-x} sites, which govern the activity, selectivity, and stability of C₂H₄ production by synergistically activating CO₂ and H₂O molecules.

The performance comparison with catalysts shown in Fig. 11(b), in terms of faradaic efficiency (FE) and partial current density, indicates that Cu₂O–5CeO_{2-C} is a promising catalytic system for C₂H₄ production. Compared to other reported catalytic systems, Cu₂O–5CeO_{2-C} demonstrates a high FE for C₂H₄ (FE_{C₂H₄} ~ 53%) at a high partial current density ($j_{\text{C}_2\text{H}_4} = 132 \text{ mA cm}^{-2}$). Additionally, one of the most significant advantages of Cu₂O–5CeO_{2-C} is that it requires a lower potential (–0.98 V vs. RHE) than the reported CeO₂/50 wt% CuO system (–2.3 V vs. RHE) to operate at the same electrolyte concentration of 1 M KOH.³³

Conclusions

This study investigated the influence of CeO₂ promotion on the catalytic performance of Cu₂O-based catalysts for the electrochemical reduction of CO₂. The addition of the CeO_{2-C} promoter phase was found to enhance the formation of C₂H₄, a valuable commercial product, during the CO₂RR compared to the non-promoted Cu₂O catalyst. The characterization techniques, including SEM, TEM, XRD, Raman spectroscopy, and X-ray photoelectron spectroscopy, provided valuable insights into the structural and compositional properties of the catalysts.

The results indicated that the synthesized catalysts exhibited well-defined morphologies, with cubic-like particles for Cu₂O and CeO_{2-C}, and rod-like morphologies for CeO_{2-R}. The XRD analysis confirmed the phase of Cu₂O and CeO₂, while Raman spectroscopy revealed characteristic peaks for both materials and a new peak indicating the interaction between Cu⁺ and Ce³⁺ cations. X-ray photoelectron spectroscopy further confirmed the presence of different copper oxidation states in the Cu₂O-based catalysts.

The electrochemical evaluation of the catalysts demonstrated that the CeO_{2-C}-promoted Cu₂O-based gas diffusion electrodes (GDEs) exhibited higher faradaic efficiencies for C₂H₄ production compared to the non-promoted Cu₂O GDE. The optimal loading of CeO_{2-C} for maximum C₂H₄ production was determined to be 5 wt%. The proposed Cu₂O–5CeO_{2-C} GDE demonstrates enhanced and stable C₂H₄ production through the interaction of Cu₂O and CeO₂, creating active sites (Cu^x–CeO_{2-x}; Cu^x = Cu²⁺, Cu⁺, Cu⁰) for the CO₂RR. It exhibits high faradaic efficiency (FE_{C₂H₄} ~ 53%) and partial current density ($j_{\text{C}_2\text{H}_4} = 132 \text{ mA cm}^{-2}$) at a low potential (–0.98 V vs. RHE) with 1 M KOH electrolyte, making it a promising catalyst. As an important fact, the FEs for C₂H₄ in the Cu₂O–5CeO_{2-C} GDE were found to be influenced by the type of electrolyte and its concentration.

These findings highlight the potential of CeO₂ promotion in improving the selectivity and activity of Cu₂O-based catalysts for the CO₂RR. The study contributes to the understanding of the structure–property relationship in CO₂ electrochemical conversion and provides a foundation for further development of more efficient catalysts.

Conflicts of interest

There are no conflicts to declare.

Acknowledgements

This work was funded by AEI projects PID2019-108136RB-C33 and CNS2022-135235 (MCIN/AEI/10.13039/501100011033 and NextGenerationEU/PRTR). A. A. acknowledges the support from the Margarita Salas grant from the European Union – Next Generation EU through the Universitat de Barcelona.

References

- 1 C. Pappijn, M. Ruitenbeek, M. F. Reyniers and K. Van Geem, *Front. Energy Res.*, 2020, **8**, 557466.
- 2 G. L. De Gregorio, T. Burdyny, A. Loiudice, P. Iyengar, W. A. Smith and R. Buonsanti, *ACS Catal.*, 2020, **10**, 4854–4862.
- 3 B. Zhang, J. Zhang, M. Hua, Q. Wan, Z. Su, X. Tan, L. Liu, F. Zhang, G. Chen, D. Tan, X. Cheng, B. Han, L. Zheng and G. Mo, *J. Am. Chem. Soc.*, 2020, **142**, 13606–13613.
- 4 J. Kim, W. Choi, J. W. Park, C. Kim, M. Kim and H. Song, *J. Am. Chem. Soc.*, 2019, **141**, 6986–6994.
- 5 D. Tan, J. Zhang, L. Yao, X. Tan, X. Cheng, Q. Wan, B. Han, L. Zheng and J. Zhang, *Nano Res.*, 2020, **13**, 768–774.
- 6 A. Zahid, A. Shah and I. Shah, *Nanomaterials*, 2022, **12**, 1380.
- 7 W. Liu, P. Zhai, A. Li, B. Wei, K. Si, Y. Wei, X. Wang, G. Zhu, Q. Chen, X. Gu, R. Zhang, W. Zhou and Y. Gong, *Nat. Commun.*, 2022, **13**, 1877.
- 8 Y. Jiang, C. Choi, S. Hong, S. Chu, T. S. Wu, Y. L. Soo, L. Hao, Y. Jung and Z. Sun, *Cell Rep. Phys. Sci.*, 2021, **2**, 100356.



- 9 W. Fu, Z. Liu, T. Wang, J. Liang, S. Duan, L. Xie, J. Han and Q. Li, *ACS Sustainable Chem. Eng.*, 2020, **8**, 15223–15229.
- 10 W. Lin, H. Chen, Z. Li, K. Sasaki, S. Yao, Z. Zhang, J. Li and J. Fu, *ChemSusChem*, 2021, **14**, 3190–3197.
- 11 R. M. Arán-Ais, F. Scholten, S. Kunze, R. Rizo and B. Roldan Cuenya, *Nat. Energy*, 2020, **5**, 317–325.
- 12 Q. Zhu, X. Sun, D. Yang, J. Ma, X. Kang, L. Zheng, J. Zhang, Z. Wu and B. Han, *Nat. Commun.*, 2019, **10**, 3851.
- 13 Y. Gao, Q. Wu, X. Liang, Z. Wang, Z. Zheng, P. Wang, Y. Liu, Y. Dai, M. Whangbo and B. Huang, *Adv. Sci.*, 2020, **7**, 1902820.
- 14 J. Bugayong and G. L. Griffin, *ECS Trans.*, 2013, **58**, 81–89.
- 15 A. Vasileff, C. Xu, Y. Jiao, Y. Zheng and S. Z. Qiao, *Chem*, 2018, **4**, 1809–1831.
- 16 X. Wang, S. Liu, H. Zhang, S. Zhang, G. Meng, Q. Liu, Z. Sun, J. Luo and X. Liu, *Chem. Commun.*, 2022, **58**, 7654–7657.
- 17 X. Zhao, H. Xie, B. Deng, L. Wang, Y. Li and F. Dong, *Chem. Commun.*, 2024, **60**, 542–545.
- 18 J. Wang, Z. Li, C. Dong, Y. Feng, J. Yang, H. Liu and X. Du, *ACS Appl. Mater. Interfaces*, 2019, **11**, 2763–2767.
- 19 D. Meng, M. Zhang, D. Si, M. Mao, Y. Hou, Y. Huang and R. Cao, *Angew. Chem., Int. Ed.*, 2021, **60**, 25485–25492.
- 20 T. T. H. Hoang, S. Verma, S. Ma, T. T. Fister, J. Timoshenko, A. I. Frenkel, P. J. A. Kenis and A. A. Gewirth, *J. Am. Chem. Soc.*, 2018, **140**, 5791–5797.
- 21 I. Merino-Garcia, J. Albo, J. Solla-Gullón, V. Montiel and A. Irabien, *J. CO₂ Util.*, 2019, **31**, 135–142.
- 22 A. Alarcón, J. Guilera, R. Soto and T. Andreu, *Appl. Catal., B*, 2020, **263**, 118346.
- 23 T. Montini, M. Melchionna, M. Monai and P. Fornasiero, *Chem. Rev.*, 2016, **116**, 5987–6041.
- 24 F. Wang, M. Wei, D. G. Evans and X. Duan, *J. Mater. Chem. A*, 2016, **4**, 5773–5783.
- 25 C. Yang, Y. Lu, L. Zhang, Z. Kong, T. Yang, L. Tao, Y. Zou and S. Wang, *Small Struct.*, 2021, **2**, 2100058.
- 26 S. B. Varandili, J. Huang, E. Oveis, G. L. De Gregorio, M. Mensi, M. Strach, J. Vavra, C. Gadiyar, A. Bhowmik and R. Buonsanti, *ACS Catal.*, 2019, **9**, 5035–5046.
- 27 X. Zong, J. Zhang, J. Zhang, W. Luo, A. Züttel and Y. Xiong, *Electrochem. Commun.*, 2020, **114**, 106716.
- 28 Z. Zhao, X. Li, J. Wang, X. Lv and H. Bin Wu, *J. CO₂ Util.*, 2021, **54**, 101741.
- 29 X. Yan, C. Chen, Y. Wu, S. Liu, Y. Chen, R. Feng, J. Zhang and B. Han, *Chem. Sci.*, 2021, **12**, 6638–6645.
- 30 S. Chu, X. Yan, C. Choi, S. Hong, A. W. Robertson, J. Masa, B. Han, Y. Jung and Z. Sun, *Green Chem.*, 2020, **22**, 6540–6546.
- 31 S. L. Chu, X. Li, A. W. Robertson and Z. Y. Sun, *Acta Phys.-Chim. Sin.*, 2021, **37**, 2009023.
- 32 J. Shan, Y. Shi, H. Li, Z. Chen, C. Sun, Y. Shuai and Z. Wang, *Chem. Eng. J.*, 2022, **433**, 133769.
- 33 S. Wang, H. Chen, W. Lin, W. Zhou, X. Lv, J. Wang and J. Fu, *Ind. Eng. Chem. Res.*, 2022, **61**, 16445–16452.
- 34 R. M. Arán-Ais, R. Rizo, P. Grosse, G. Algara-Siller, K. Dembélé, M. Plodinec, T. Lunkenbein, S. W. Chee and B. Roldan Cuenya, *Nat. Commun.*, 2020, **11**, 3489.
- 35 S. C. Perry, S. M. Gateman, R. Malpass-Evans, N. McKeown, M. Wegener, P. Nazarovs, J. Mauzeroll, L. Wang and C. Ponce de León, *Chemosphere*, 2020, **248**, 125993.
- 36 S. Lorient, *Catal. Today*, 2021, **373**, 98–111.
- 37 N. Kainbayev, M. Sriubas, D. Virbukas, Z. Rutkunienė, K. Bockute, S. Bolegenova and G. Laukaitis, *Coatings*, 2020, **10**, 432.
- 38 C. Schilling, A. Hofmann, C. Hess and M. V. Ganduglia-Pirovano, *J. Phys. Chem. C*, 2017, **121**, 20834–20849.
- 39 E. Sartoretti, C. Novara, F. Giorgis, M. Piumetti, S. Bensaid, N. Russo and D. Fino, *Sci. Rep.*, 2019, **9**, 3875.
- 40 R. Zamiri, H. Abbastabar Ahangar, A. Kaushal, A. Zakaria, G. Zamiri, D. Tobaldi and J. M. F. Ferreira, *PLoS One*, 2015, **10**, e0122989.
- 41 H. Solache-Carranco, G. Juárez-Díaz, M. Galván-Arellano, J. Martínez-Juárez, G. Romero-Paredes and R. Peña-Sierra, in 5th International Conference on Electrical Engineering, Computing Science and Automatic Control (CCE 2008), IEEE, 2008.
- 42 A. Singhal, M. R. Pai, R. Rao, K. T. Pillai, I. Lieberwirth and A. K. Tyagi, *Eur. J. Inorg. Chem.*, 2013, 2640–2651.
- 43 A. Sahai, N. Goswami, S. D. Kaushik and S. Tripathi, *Appl. Surf. Sci.*, 2016, **390**, 974–983.
- 44 C. Lu, Z. Li, L. Ren, N. Su, D. Lu and Z. Liu, *Sensors*, 2019, **19**, 2926.
- 45 L.-C. Chen, C.-C. Chen, K.-C. Liang, S. H. Chang, Z.-L. Tseng, S.-C. Yeh, C.-T. Chen, W.-T. Wu and C.-G. Wu, *Nanoscale Res. Lett.*, 2016, **11**, 402.
- 46 M. Dosa, M. Piumetti, S. Bensaid, T. Andana, C. Novara, F. Giorgis, D. Fino and N. Russo, *Catal. Lett.*, 2018, **148**, 298–311.
- 47 A. Nakajima, A. Yoshihara and M. Ishigame, *Phys. Rev.*, 1994, **50**(18), 13297–13307.
- 48 Y. Wang, Y. Lü, W. Zhan, Z. Xie, Q. Kuang and L. Zheng, *J. Mater. Chem. A*, 2015, **3**, 12796–12803.
- 49 Y. Tian, X. Fei, H. Ning, W. Wang, X. Tan, X. Wang, Z. Ma, Z. Guo and M. Wu, *Front. Chem.*, 2022, **10**, 915759.
- 50 Y. Wang, Y. Lü, W. Zhan, Z. Xie, Q. Kuang and L. Zheng, *J. Mater. Chem. A*, 2015, **3**, 12796–12803.
- 51 A. Dey, G. Chandrabose, L. A. O. Dampthey, E. S. Erakulan, R. Thapa, S. Zhuk, G. K. Dalapati, S. Ramakrishna, N. S. J. Braithwaite, A. Shirzadi and S. Krishnamurthy, *Appl. Surf. Sci.*, 2021, **541**, 148571.
- 52 Z. Gu, N. Yang, P. Han, M. Kuang, B. Mei, Z. Jiang, J. Zhong, L. Li and G. Zheng, *Small Methods*, 2019, **3**, 1800449.
- 53 T. Wei, S. Zhang, Q. Liu, Y. Qiu, J. Luo and X. Liu, *Acta Phys.-Chim. Sin.*, 2022, 202207026.
- 54 Y. Wu, C. Chen, X. Yan, S. Liu, M. Chu, H. Wu, J. Ma and B. Han, *Green Chem.*, 2020, **22**, 6340–6344.

